

# Dense granular flow rheology in turbulent bedload transport

Raphael Maurin<sup>1</sup>†, Julien Chauchat<sup>2</sup>‡, and Philippe Frey<sup>1</sup>

<sup>1</sup>Univ. Grenoble Alpes, Irstea, UR ETGR, 2 rue de la Papeterie-BP 76, F-38402 St-Martin-d'Hères, France

<sup>2</sup>Univ. Grenoble Alpes, LEGI, G-INP,CNRS, F-38000 Grenoble, France

(Received xx; revised xx; accepted xx)

The local granular rheology is investigated numerically in turbulent bedload transport. Considering spherical particles, steady uniform configurations are simulated using a coupled fluid-discrete-element model. The stress tensor is computed as a function of the depth for a series of simulations varying the Shields number, the specific density and the particle diameter. The results are analyzed in the framework of the  $\mu(I)$  rheology and exhibit a collapse of both the shear to normal stress ratio and the solid volume fraction over a wide range of inertial numbers. Contrary to expectations, the effect of the interstitial fluid on the granular rheology is shown to be negligible, supporting recent work suggesting the absence of a clear transition between the free-fall and turbulent regime. In addition, data collapse is observed up to unexpectedly high inertial numbers  $I \sim 2$ , challenging the existing conceptions and parametrization of the  $\mu(I)$  rheology. Focusing upon bedload transport modelling, the results are pragmatically analyzed in the  $\mu(I)$  framework in order to propose a granular rheology for bedload transport. The proposed rheology is tested using a 1D volume-averaged two-phase continuous model, and is shown to accurately reproduce the dense granular flow profiles and the sediment transport rate over a wide range of Shields numbers. The present contribution represents a step in the upscaling process from particle-scale simulations toward large-scale applications involving complex flow geometry.

**Key words:** Sediment transport, granular media, rheology

## 1. Introduction

Among the different regimes of sediment transport, bedload transport is of major importance as it represents an important contribution to river morphology evolution. Accordingly, prediction of the sediment transport rate under turbulent bedload conditions is fundamental for preventing environmental risks associated with floods and scouring. From a physical point of view, bedload transport corresponds to the dynamic response of a granular bed submitted to a fluid shear stress. In contrast to suspended load, bedload is defined as the part of the sediment load occurring close to the granular bed in which particles are in permanent or intermittent contact with the bed (Fredsoe & Deigaard 1992).

The sediment transport rate is usually quantified in dimensionless form using the so-called Einstein number (Einstein 1942),  $Q_s^* = Q_s/[d\sqrt{(\rho^p/\rho^f - 1)gd}]$ , where  $Q_s$  represents the volumetric sediment transport rate per unit width,  $\rho^p$  and  $\rho^f$  are the

† Present address: Université de Toulouse, INPT, UPS, IMFT (Institut de Mécanique des Fluides de Toulouse), Allée Camille Soula, F-31400 Toulouse, France

‡ Email address for correspondence: julien.chauchat@grenoble-inp.fr

particle and fluid densities,  $g$  is the acceleration of gravity and  $d$  is the particle diameter. In the hydraulic community the classical way to model bedload transport consists of assuming a power law relation between the Einstein number and the Shields number  $\theta$ . The latter corresponds to the ratio of the traction force exerted by the fluid at the bed  $\tau^f d^2$  and the buoyant weight of a single particle  $(\rho^p - \rho^f)gd^3$ , i.e.  $\theta = \tau^f / [(\rho^p - \rho^f)gd]$ . Given the lack of accuracy of the classical formulae (e.g. Meyer-Peter & Müller (1948)), renewed attention has recently been given to the granular phase behaviour in bedload transport (Frey & Church 2009, 2011) from both an experimental (Mouilleron *et al.* 2009; Hergault *et al.* 2010; Lajeunesse *et al.* 2010; Frey 2014; Aussillous *et al.* 2013; Houssais *et al.* 2015) and a numerical point of view (Duran *et al.* 2012; Ji *et al.* 2013; Kidanemariam & Uhlmann 2014; Maurin *et al.* 2015).

The granular rheology characterises the response of the granular medium, in terms of deformation rate, to a given external stress and vice-versa. It is usually given as the relation between the granular stress and strain rate tensors. In bedload transport, the granular rheology governs both the response to, and the interaction with the fluid shear stress. Its knowledge is required for two-phase flow models in which both the fluid and solid phases are considered as continuous (Eulerian-Eulerian) (e.g. Aussillous *et al.* (2013)). As such it represents an important step in the upscaling of sediment transport processes from Eulerian-Lagrangian models to Eulerian-Eulerian models, which enable numerical simulations of larger-scale problems and/or complex flow forcings.

Under bedload transport conditions, the granular medium experiences all of the granular flow regimes, from quasi-static in the sediment bed to dilute rapid granular flows in the upper sediment transport layer. The dilute rapid and dense granular flow regimes have mainly been described using the kinetic theory of granular flows and the  $\mu(I)$  rheology respectively. The former is based on the analogy of dilute granular flows with molecular gases, assuming binary collisions. It has been proven to accurately describe rapid dilute granular flows in different configurations (Campbell 1990; Goldhirsch 2003), and has recently been extended to the dense granular flow regime (Jenkins 2006, 2007; Berzi *et al.* 2011). Alternatively, the  $\mu(I)$  local rheology accurately describes the dense granular flow regimes and is based on the dimensional analysis of the simple shear configuration (Midi 2004; Forterre & Pouliquen 2008; Jop 2015). In the latter case, the unique dimensionless number controlling the system is the so-called inertial number (Da Cruz *et al.* 2005):

$$I = \dot{\gamma}d\sqrt{\rho^p/P^p}, \quad (1.1)$$

with  $P^p$  the confining granular pressure and  $\dot{\gamma}$  the granular shear rate. This dimensionless number can be interpreted as the ratio between a macroscopic time scale of deformation  $t_{macro} = 1/\dot{\gamma}$  and a microscopic time scale of rearrangement  $t_{micro} = d/\sqrt{P^p/\rho^p}$ . From the dimensional analysis, the dimensionless solid volume fraction  $\phi$  and shear to normal granular stress ratio  $\mu = \tau^p/P^p$  are unique functions of the inertial number  $I$ . From experiments and numerical simulations, they can be expressed as (Da Cruz *et al.* 2005; Jop *et al.* 2006)

$$\frac{\tau^p}{P^p} = \mu(I) = \mu_s + \frac{\mu_2 - \mu_s}{1 + I_0/I}, \quad (1.2)$$

$$\phi(I) = \phi^{max} - aI, \quad (1.3)$$

where  $\phi^{max}$  is the maximum packing fraction,  $\mu_s$  is the static effective granular friction coefficient, and  $\mu_2$ ,  $I_0$  and  $a$  are phenomenological constants. By combining the different

expressions (eq. 1.1-1.3), the granular stress tensor can be expressed as a function of the shear rate, defining the granular rheology.

Based on the simple shear configuration, the  $\mu(I)$  rheology has been extended to account for the presence of interstitial fluids (Courrech du Pont *et al.* 2003; Cassar *et al.* 2005). Considering rearrangement time scales according to the dominant mechanism, three regimes can be defined by introducing two dimensionless numbers (Courrech du Pont *et al.* 2003; Cassar *et al.* 2005; Andreotti *et al.* 2013), with  $C_D$  the drag coefficient,

$$St = \frac{d\sqrt{\rho^p P^p}}{\eta^f}, \quad (1.4)$$

$$r = \sqrt{\frac{\rho^p}{\rho^f C_D}}, \quad (1.5)$$

the free-fall regime ( $St \gg 1$ ,  $r \gg 1$ ) corresponding to negligible influence of the interstitial fluid (i.e. dry granular media), the viscous regime ( $St \ll 1$ ,  $r \ll 1$ ) corresponding to a rearrangement time scale dominated by viscous drag and the turbulent regime ( $St \gg 1$ ,  $r \ll 1$ ) corresponding to a rearrangement time scale dominated by fluid inertial effects. In the different regimes, the results therefore scale with the dry inertial number  $I_{dry} = \dot{\gamma}d\sqrt{\rho^p/P^p}$ , the turbulent one  $I_{turb} = \dot{\gamma}d\sqrt{\rho^f C_D/P^p}$  and the viscous one  $I_{visc} = \eta^f \dot{\gamma}/P^p$  respectively. This approach has been applied with some success to various complex immersed configurations from avalanches (Courrech du Pont *et al.* 2003; Cassar *et al.* 2005; Doppler *et al.* 2007), to granular collapses (Rondon *et al.* 2011; Izard *et al.* 2014), annular shear cells (Boyer *et al.* 2011; Trulsson *et al.* 2012) and sediment transport (Ouriemi *et al.* 2009; Revil-Baudard & Chauchat 2013; Aussillous *et al.* 2013; Chiodi *et al.* 2014).

To the best of our knowledge, there are only a few contributions in the literature on the dense granular flow rheology in the context of bedload transport. Ouriemi *et al.* (2009) and Aussillous *et al.* (2013) have studied laminar bedload in closed conducts using refractive index-matching experiments and theoretical two-phase continuous models. Assuming a constant solid volume fraction and a limited transitional layer from dense to dilute granular flow, the authors have shown that the  $\mu(I)$  rheology gives excellent agreement with experimental data. It is worth noting that in the laminar case, the lag between the fluid and solid velocities is negligible (Mouilleron *et al.* 2009; Aussillous *et al.* 2013), the two phases being tightly coupled. In intense turbulent bedload transport, termed sheet flow, the transitional layer from dense to dilute granular flows and the fluid-particle velocity lag are more important (Sumer *et al.* 1996; Cowen *et al.* 2010; Revil-Baudard *et al.* 2015). This regime has been studied experimentally (Capart & Fraccarollo 2011) and numerically using the two-phase flow continuous modelling framework with the kinetic theory of granular flows (Jenkins & Hanes 1998; Hsu *et al.* 2004) and the  $\mu(I)$  rheology (Revil-Baudard & Chauchat 2013; Chauchat *et al.* 2015). While the agreement of the numerical simulations with the available experimental data gives some credit to both granular rheologies, recent experimental investigations by Revil-Baudard *et al.* (2015) showed that the solid volume fraction profiles observed were substantially different from the predicted ones. The observed effective friction coefficient also differs importantly from the classical values used in the  $\mu(I)$  rheology, possibly due to the strong intermittency induced by the turbulent coherent structures (Revil-Baudard *et al.* 2015). At the transition from sheet flows to debris flow, the granular rheology has been used to model steep slope configurations (Armanini *et al.* 2005; Larcher *et al.* 2007;

Berzi & Jenkins 2008; Armanini *et al.* 2014). Combining experimental particle tracking at the wall (Armanini *et al.* 2005; Larcher *et al.* 2007) and numerical analysis (Berzi & Jenkins 2008; Armanini *et al.* 2014), both the  $\mu(I)$  rheology (Berzi & Jenkins 2008) and hybrid  $\mu(I)$ -kinetic theory models (Armanini *et al.* 2014) have been shown to accurately describe the granular behaviour in this configuration.

The literature review underlines the relevance of both the kinetic theory and the dense granular flow rheology for bedload transport modelling. However, the numerical studies are restricted to continuous two-phase analysis and the experimental evaluations of the granular stress tensor rely on solid volume fraction measurements that are highly uncertain. In addition, while direct numerical simulations (DNS) have been performed at the particle scale in the laminar regime (Kidanemariam & Uhlmann 2014), this type of numerical model is not affordable for turbulent bedload transport due to the typical values of bulk Reynolds numbers explored. Therefore, to go beyond the existing two-phase continuous numerical works, the present paper analyses the local granular rheology in turbulent bedload transport using a coupled fluid-discrete-element model (DEM) with a volume-averaged fluid description (Maurin *et al.* 2015). This approach permits local computation of the granular stress tensor and the granular shear rate, bringing new insights into the local granular behaviour in turbulent bedload transport. Based on these Eulerian-Lagrangian simulations a dense granular flow rheology for bedload transport is proposed and further tested in a two-phase continuous (Eulerian-Eulerian) model. Besides, bedload transport configurations enable local analysis of the granular rheology in complex immersed granular flows, and the DEM results are shown to be of interest for granular media in general.

The paper is structured as follows. First, the coupled fluid-DEM and two-phase continuous models are briefly presented (section 2). Then, fluid-DEM simulations are analyzed in the framework of the dense granular flow  $\mu(I)$  rheology (section 3). Finally, extending the simulations to realistic conditions for bedload transport, a parametrization of the  $\mu(I)$  rheology is proposed from the DEM results, and is tested with the two-phase continuous model (section 4).

## 2. Model formulation

The Eulerian-Lagrangian and Eulerian-Eulerian models are based on the same volume-averaged two-phase flow equations for the fluid phase. The solid phase is modelled on the one hand as a continuum (Eulerian-Eulerian) and on the other hand using a 3D DEM in which each particle motion is computed explicitly (Eulerian-Lagrangian). Both two-phase flow models have already been described and validated with experiments (Maurin *et al.* 2015; Chauchat *et al.* 2015) and only a brief description will be given. The reader is referred to the abovementioned references for a complete description of the model formulations and validations.

Considering steady uniform conditions, the problem is unidirectional so that the average fluid and solid velocities depend only on the wall-normal direction and reduce to their streamwise components  $\langle \mathbf{u} \rangle^f = \langle u_x \rangle^f(z) \mathbf{e}_x$  and  $\langle \mathbf{v}^p \rangle^s = \langle v_x^p \rangle^s(z) \mathbf{e}_x$ . Therefore, the streamwise and wall-normal volume-averaged fluid phase momentum balances are

given by (Anderson & Jackson 1967; Jackson 2000; Revil-Baudard & Chauchat 2013)

$$0 = \frac{\partial S_{xz}^f}{\partial z} + \frac{\partial R_{xz}^f}{\partial z} + \rho^f (1 - \phi) g \sin \alpha - n \langle f_x \rangle^p, \quad (2.1)$$

$$0 = -\frac{\partial P^f}{\partial z} + \rho^f (1 - \phi) g \cos \alpha - n \langle f_z \rangle^p, \quad (2.2)$$

where  $\sigma_{ij}^f = -P^f \delta_{ij} + S_{ij}^f$  is the volume-averaged effective viscous stress tensor,  $R_{xz}^f$  is the Reynolds shear stress tensor,  $\phi$  is the solid phase volume fraction,  $\langle f_k \rangle^p$  is the volume-averaged fluid-particle interaction force,  $n = \phi / (\pi d^3 / 6)$  is the number density of particles and  $\alpha$  is the channel inclination angle. Omitting the model-dependent fluid-particle interaction force, the solution of the fluid momentum balance requires closure laws for the viscous shear stress tensor and the Reynolds stress tensor.

Considering a Newtonian fluid, the viscous shear stress is classically expressed as

$$S_{xz}^f = \rho^f (1 - \phi) \nu^f \frac{d \langle u_x \rangle^f}{dz}, \quad (2.3)$$

with  $\nu^f$  the clear fluid kinematic viscosity and  $\langle u_x \rangle^f$  the volume-averaged streamwise fluid phase velocity. The Reynolds shear stress is based on the eddy viscosity concept ( $\nu^t$ ) using a mixing length formulation:

$$R_{xz}^f = \rho^f \nu^t \frac{d \langle u_x \rangle^f}{dz} \quad \text{with} \quad \nu^t = (1 - \phi) l_m^2 \left| \frac{d \langle u_x \rangle^f}{dz} \right|, \quad (2.4)$$

where the mixing length is taken similarly to Li & Sawamoto (1995) as

$$l_m(z) = \kappa \int_0^z \frac{\phi^{max} - \phi(\zeta)}{\phi^{max}} d\zeta, \quad (2.5)$$

with  $\kappa = 0.41$  the von Karman constant. The formulation adopted allows one to recover the law of the wall (Prandtl 1926) in clear fluid, while the turbulence is completely damped inside the granular bed at maximum packing fraction ( $\phi^{max}$ ).

### 2.1. Eulerian-Lagrangian model

The Eulerian-Lagrangian model is based on the explicit solution of the dynamic equation for each individual particle using the 3D DEM open-source code YADE (Šmilauer et al. 2015). The DEM solution is spatially averaged and explicitly coupled with the fluid phase momentum balance equations (2.1-2.2) through the drag term  $n \langle f_x^D \rangle^p$  and the solid volume fraction  $\phi$ .

For each particle  $p$  at position  $\mathbf{x}^p$ , the Newton equations are solved considering nearest-neighbours interactions:

$$m \frac{d^2 \mathbf{x}^p}{dt^2} = \sum_{k \in \mathcal{N}} \mathbf{f}_c^{pk} + \mathbf{f}_{ext} = \sum_{k \in \mathcal{N}} \mathbf{f}_c^{pk} + \mathbf{f}_g^p + \mathbf{f}_b^p + \mathbf{f}_D^p \quad (2.6)$$

where the sum of the contact forces  $\mathbf{f}_c^{pk}$  is made over the ensemble of nearest neighbours  $\mathcal{N}$ ,  $\mathbf{f}_g^p$  is the gravity force,  $\mathbf{f}_b^p$  is the buoyancy force and  $\mathbf{f}_D^p$  is the 3D drag force applied by the fluid on particle  $p$ . For each contact, the contact force is computed explicitly using

the classical spring-dashpot contact law (Schwager & Pöschel 2007):

$$F_n = -k_n \delta_n - c_n \dot{\delta}_n \quad (2.7a)$$

$$F_t = -\min(k_s \delta_t, \mu^p F_n), \quad (2.7b)$$

where  $F_n$  and  $F_t$  are the normal and tangential contact forces between particle  $p$  and  $k$ ,  $\delta_n$  and  $\delta_t$  are the normal and tangential overlaps,  $k_n$  and  $k_s$  are the normal and tangential contact stiffnesses,  $c_n$  is the normal viscous damping and  $\mu^p$  is the tangential friction coefficient. This contact law is well suited for granular flow analysis and allows one to define a unique restitution coefficient  $e_n$  (Schwager & Pöschel 2007). Similarly, the rotation of the particles is solved from the Newton equations of motion.

The interaction with the fluid phase is restricted to buoyancy and drag forces:

$$\mathbf{f}_b^p = -\frac{\pi d^3}{6} \nabla P^f, \quad (2.8)$$

$$\mathbf{f}_D^p = \frac{1}{2} \rho^f \frac{\pi d^2}{4} C_D \left\| \langle \mathbf{u} \rangle_{\mathbf{x}^p}^f - \mathbf{v}^p \right\| \left( \langle \mathbf{u} \rangle_{\mathbf{x}^p}^f - \mathbf{v}^p \right), \quad (2.9)$$

where the average fluid velocity and the fluid pressure are taken at the center of particle  $p$ . The drag coefficient  $C_D$  depends on the particle Reynolds number  $Re_p = \left\| \langle \mathbf{u} \rangle_{\mathbf{x}^p}^f - \mathbf{v}^p \right\| d / \nu^f$  and takes into account hindrance effects (DallaValle 1948; Richardson & Zaki 1954):  $C_D = (0.4 + 24.4/Re_p)(1 - \phi)^{-3.1}$ .

Considering steady uniform turbulent flows, the buoyancy force reduces to its wall-normal component and equation (2.2) leads to a hydrostatic fluid pressure distribution, the wall-normal average drag force being negligible. The solution of the streamwise fluid phase momentum balance (eq. 2.1) requires the evaluation of both the spatially averaged solid phase volume fraction and the momentum transmitted from the fluid to the particles through drag forces:

$$n \langle f_x^D \rangle^s = \frac{\phi}{\pi d^3 / 6} \langle f_x^D \rangle^s = \frac{3}{4} \frac{\phi \rho^f}{d} \left\langle C_D \left\| \langle \mathbf{u} \rangle^f - \mathbf{v}^p \right\| \left( \langle u_x \rangle^f - v_x^p \right) \right\rangle^s. \quad (2.10)$$

In the DEM processing, the solid phase averaging  $\langle \bullet \rangle^s$  is used instead of the particle phase averaging  $\langle \bullet \rangle^p$ . While the two are identical provided that there is scale separation (Anderson & Jackson 1967; Jackson 2000), the importance of the wall-normal gradients in bedload transport requires a weighting function length scale lower than the particle diameter in order to define an independent averaging (Maurin *et al.* 2015; Maurin 2015). Therefore, a small wall-normal weighting function length scale has been adopted (typically  $d/30$ ), and this choice has been validated through an experimental comparison (Maurin *et al.* 2015).

The 3D DEM and the fluid model are solved as transient problems applying a fixed bottom boundary condition for both the fluid ( $\langle \mathbf{u} \rangle^f(z=0) = 0$ ) and the particle phase (fixed random particles) and imposing the position of the water free-surface ( $d \langle u_x \rangle^f / dz(z=h) = 0$ ). In order to achieve a stable integration, the DEM time step is bounded by the propagation time of the fastest wave over a particle diameter (Maurin 2015; Maurin *et al.* 2015). The fluid resolution time step corresponds to a typical characteristic evolution time scale of the granular medium and is taken much larger than the DEM one (Maurin *et al.* 2015):  $\Delta t_f = 10^{-2} s$  with respect to  $\Delta t_p \sim$

$O(10^{-4} - 10^{-5})$  s. Therefore, the coupling between the fluid and granular phases ensures momentum conservation of the system on average. The model has been compared with experiments and has shown its ability to describe accurately the granular depth structure in turbulent bedload transport (Maurin *et al.* 2015).

## 2.2. Eulerian-Eulerian model

The Eulerian-Eulerian model is based on the numerical solution of the fluid phase momentum balance equations (eqs 2.1 and 2.2) coupled with the spatially averaged granular phase momentum balance equations in the streamwise and wall-normal directions. For steady uniform flow conditions the granular phase momentum equations read (Chauchat *et al.* 2015)

$$0 = \frac{\partial \tau_{xz}^p}{\partial z} + \rho^p \phi g \sin \alpha + n \langle f_x \rangle^p, \quad (2.11)$$

$$0 = -\frac{\partial P^p}{\partial z} + \rho^p \phi g \cos \alpha + n \langle f_z \rangle^p, \quad (2.12)$$

where  $\tau_{xz}^p$  is the spatially-averaged granular phase shear stress. Like in the Eulerian-Lagrangian model, the buoyancy is applied along the wall-normal direction and leads to hydrostatic pressure distribution for the granular phase. In the continuous formalism the spatially averaged streamwise drag force is given by

$$n \langle \mathbf{f}^D \rangle^s = \frac{3}{4} \frac{\phi \rho^f}{d} C_D \left\| \langle \mathbf{u} \rangle^f - \langle \mathbf{v}^p \rangle^s + \mathbf{u}_d \right\| \left( \langle \mathbf{u} \rangle^f - \langle \mathbf{v}^p \rangle^s + \mathbf{u}_d \right), \quad (2.13)$$

where the extra term  $\mathbf{u}_d$  is the drift velocity which represents the dispersion effect due to the averaged fluid-particle velocity fluctuations. This term is responsible for sediment transport suspension and allows one to reproduce the Rouse profile provided that the wall normal component is taken as:  $(u_d)_z = -\nu^t/\phi \, d\phi/dz$  (Chauchat *et al.* 2015). The streamwise component is taken as  $(u_d)_x = 0$  in this paper.

The granular shear stress tensor is modeled using the  $\mu(I)$  rheology presented in the introduction. Combining equations (1.1) and (1.2), the shear and normal components of the granular stress tensor can be expressed as

$$P^p = \frac{1}{I^2} \rho_p \, d^2 \left( \frac{d \langle v_x^p \rangle^s}{dz} \right)^2, \quad (2.14)$$

$$\tau^p = \frac{\mu(I)}{I^2} \rho_p \, d^2 \left( \frac{d \langle v_x^p \rangle^s}{dz} \right)^2. \quad (2.15)$$

Inverting equation 1.3, the inertial number is obtained as a function of the solid volume fraction and the two equations can be directly expressed as a function of the solid volume fraction and the average solid velocity gradient.

The numerical algorithm is based on a transient solution of the governing equations (2.1; 2.2; 2.11 and 2.12), together with the continuity equation for the solid phase. Fixed boundary conditions are imposed at the bottom of the sample at  $z = 0$  ( $\langle \mathbf{u} \rangle^f = 0$ ) where the granular phase is considered to be at rest ( $\langle \mathbf{v}^p \rangle^s = 0$ ,  $d\phi/dz = 0$ ), while the positions of the water and granular free-surfaces are imposed in  $z = h$  ( $d \langle u_x \rangle^f / dz = 0$ ,  $\langle u_z \rangle^f = 0$ ,  $\langle v_z^p \rangle^s = 0$ ,  $d\phi/dz = 0$ ). The governing equations are discretised using a finite volume technique for the mass conservation equation and a finite difference technique for the momentum balance. A staggered grid is used with the velocities located at the cell face and the scalar quantities (e.g. volume fractions or viscosities) located at the cell center.

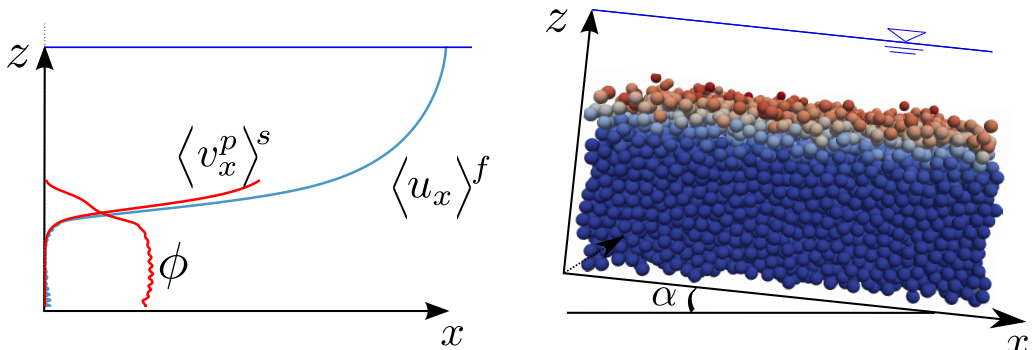


FIGURE 1. Scheme of the numerical setup and its equivalent average unidirectional picture with typical fluid velocity  $\langle \mathbf{u}^f \rangle = \langle u_x^f \rangle(z) \mathbf{e}_x$ , solid volume fraction  $\phi$ , and solid velocity  $\langle \mathbf{v} \rangle^s = \langle v_x \rangle^s(z) \mathbf{e}_x$  depth profiles. The inclined 3D bi-periodic granular description is coupled with a unidirectional fluid momentum balance using imposed fixed random bottom boundary condition and water free-surface position. The particle color is representative of the velocity intensity.

---

$\theta^*$	$Re$	$Re_p$	$\rho^p/\rho^f - 1$	$Fr$	$S^*$	$St$	$r$
$[0.04, 0.6]$	$10^3 - 10^6$	$10^3 - 10^4$	$[0.375, 1.5]$	$\gtrsim 1$	$[2, 5]$	$10^2 - 10^4$	$0.1 - 2$

---

TABLE 1. Main characteristic dimensionless numbers of the configurations considered.

For the pressure-velocity coupling a projection method is used. The numerical schemes are Euler implicit for the time derivative, upwind for the advection terms and central difference for the diffusion terms. For additional informations on the numerical model, the reader is referred to Chauchat *et al.* (2013) and Chauchat *et al.* (2015).

### 3. Results and methodology

The numerical setup of the Eulerian-Lagrangian model is presented in figure 1. It consists of a channel flow tilted with an inclination angle  $\alpha = 0.05$  rad, partially filled with monodisperse spherical particles of diameter  $d$ . The three-dimensional granular sample is biperiodic (streamwise and spanwise) and the periodic cell size is taken as  $l_x = l_y = 30d$  to ensure statistical convergence of the spatial averaging operator (Maurin *et al.* 2015). A 10-15 diameter thick granular layer is deposited under gravity over a rough random bottom, and the system evolves under gravity with a fixed water free-surface elevation. The water flow is turbulent ( $Re = U^f h/\nu^f \sim 10^4$ ), hydraulically rough ( $Re_p = U^f d/\nu^f \sim 10^3$ ) and supercritical ( $Fr = U^f/\sqrt{gh} \gtrsim 1$ ), with  $U^f$  the average fluid velocity within the water depth  $h$ . The results are independent of the granular bottom boundary conditions in the range of parameters investigated (Maurin 2015) and the simulations are performed in the rigid grain limit (Roux & Combe 2002) with a tangential stiffness set to half the normal one. The friction coefficient is set to a realistic value for glass beads,  $\mu^p = 0.4$ , and the restitution coefficient is taken as  $e_n = 0.5$  to account for the lubrication effect consistently with the experimental validation (Maurin *et al.* 2015).

In order to define properly an equivalent continuous medium for the granular phase, the analysis is restricted, in a first approach, to cases with a non-negligible number of particle



---

Run	$\rho^p/\rho^f - 1$	$d(mm)$	$\theta^*$	symbol
r0d3s1	0.375	3	0.214	●
r0d3s2	0.375	3	0.444	●
r0d3s3	0.375	3	0.611	●
r0d6s1	0.375	6	0.215	+
r0d6s2	0.375	6	0.44	+
r0d6s3	0.375	6	0.598	+
r0d12s1	0.375	12	0.216	x
r0d12s2	0.375	12	0.434	x
r0d12s3	0.375	12	0.593	x
r1d3s1	0.75	3	0.188	●
r1d3s2	0.75	3	0.378	●
r1d3s3	0.75	3	0.593	●
r1d6s1	0.75	6	0.193	+
r1d6s2	0.75	6	0.381	+
r1d6s3	0.75	6	0.598	+
r1d12s1	0.75	12	0.191	x
r1d12s2	0.75	12	0.379	x
r1d12s3	0.75	12	0.596	x
r2d3s1	1.5	3	0.205	●
r2d3s2	1.5	3	0.443	●
r2d3s3	1.5	3	0.694	●
r2d6s1	1.5	6	0.205	+
r2d6s2	1.5	6	0.455	+
r2d6s3	1.5	6	0.692	+
r2d12s1	1.5	12	0.21	x
r2d12s2	1.5	12	0.451	x
r2d12s3	1.5	12	0.696	x

---

TABLE 2. Parameters of the simulations studied and symbol correspondence. The specific density, particle diameter, and Shields number have been varied. The latter is evaluated from the maximum of the turbulent shear stress, using  $\tau^f = \max(R_{xz}^f) = \rho^f u_*^2$ . Each specific density is associated with a color, which intensity reflects the Shields number. The symbol associated with the run is characteristic of the particle diameter.

---

layers in motion. The range of Shields numbers investigated has been chosen between  $\theta^* \sim 0.2$  and  $\theta^* \sim 0.6$ , to prevent suspended load and stay in the bedload regime by keeping high suspension numbers ( $S^* = w_s/u_* \in [2, 5]$ ). For mountain stream bedload, this represents intense rare events with high transport capacity. It can also be seen as a limit case of sheet flow without suspension. In order to investigate the scaling laws, the Shields number, the specific density and the particle diameter are varied. For each parameter, three values are considered starting from a realistic case for intense bedload transport ( $\theta^* \sim 0.4$ ,  $\rho^p/\rho^f - 1 = 1.5$ ,  $d = 6mm$ ), corresponding to the particle density and diameter used for the experimental validation (Maurin *et al.* 2015). The specific density is lowered starting from  $\rho^p/\rho^f - 1 = 1.5$ , considering that experimental data are often made with plastic in sheet flows (e.g. Capart & Fraccarollo (2011); Revil-Baudard *et al.* (2015)). The main characteristic dimensionless numbers of the problem are shown in table 1 and the exact parameters investigated are given in table 2. For each run, once the system is at steady state, the data measured every 0.1s are averaged over time for 300s for post-processing.

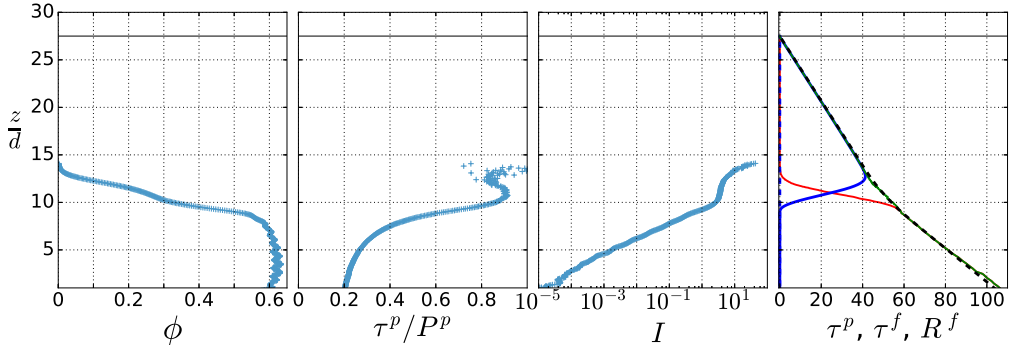


FIGURE 2. Representative example (case r2d6s2 in table 2) of solid volume fraction, shear to normal granular stress ratio, inertial number, and total stress repartition depth profiles. The last panel shows the different components of the mixture momentum balance as a function of the depth, as derived in appendix A: the granular shear stress (—), the Reynolds shear stress (---), the viscous shear stress (- - -), the sum of the three (- · -), and the slope contribution (last term of equation A 4, - - -). The water free-surface elevation is represented in each different panel for reference (—).

### 3.1. Methodology

In order to study the granular rheology, the granular stress tensor is computed from the 3D DEM results by applying the spatial averaging operator to the granular stress tensor. Therefore,  $\langle \sigma_{ij}^p \rangle^s$  is obtained for each slice of volume  $V$  by computing (Goldhirsch 2010; Andreotti *et al.* 2013)

$$\langle \sigma_{ij}^p \rangle^s = -P^p \delta_{ij} + \tau_{ij}^p = -\frac{1}{V} \sum_{\beta \in V} m^\beta v_i^{\prime\beta} v_j^{\prime\beta} - \frac{1}{V} \sum_{(m,n) \in V} f_c^{m,n} b_j^{m,n}, \quad (3.1)$$

where the sums are respectively over the particles and the contacts contained in the volume  $V$ ,  $v_k^{\prime\beta} = v_k^\beta - \langle v_k \rangle$  is the  $k^{\text{th}}$  component of the spatial velocity fluctuation associated with particle  $\beta$  of mass  $m^\beta$ ,  $\mathbf{f}_c^{m,n}$  is the contact force applied by particle  $m$  on particle  $n$  and  $\mathbf{b}^{m,n}$  is the branch vector from particle  $m$  to particle  $n$ .

Considering the unidirectional character of the problem, the weighting function of the spatial averaging operator extends over the whole width and length of the periodic cell. Therefore, one obtains for each run time-averaged depth profiles of the shear and normal granular stress components:  $\tau^p(z) = \tau_{xz}^p(z)$  and  $P^p(z) = \tau_{zz}^p(z)$ . Negligible stress asymmetry and compensated normal stress difference have been observed (Maurin 2015). Figure 2 presents typical depth profiles for a given representative simulation (run r2d6s2 in table 2). The last panel shows the different components of the streamwise mixture momentum balance, as derived in appendix A. Similarly to Revil-Baudard & Chauchat (2013) in the sheet flow regime, the viscous stress tensor contribution is found to be negligible in turbulent bedload transport. In addition, the momentum balance is closed at each elevation, as the streamwise projection of the gravity contribution is balanced by the sum of the other terms, showing the consistency of the model formulation and stress tensor evaluation. The depth profile of the inertial number (figure 2) shows that a very important range of inertial numbers (approximately five orders of magnitude) is sampled as a function of the depth in a single simulation. This is due to the nature of bedload transport in which the granular flow evolves from quasi-static in the bed to very dynamic at the granular free-surface. As the shear to normal stress ratio and the solid volume fraction vary accordingly throughout the depth (see figure 2), this allows

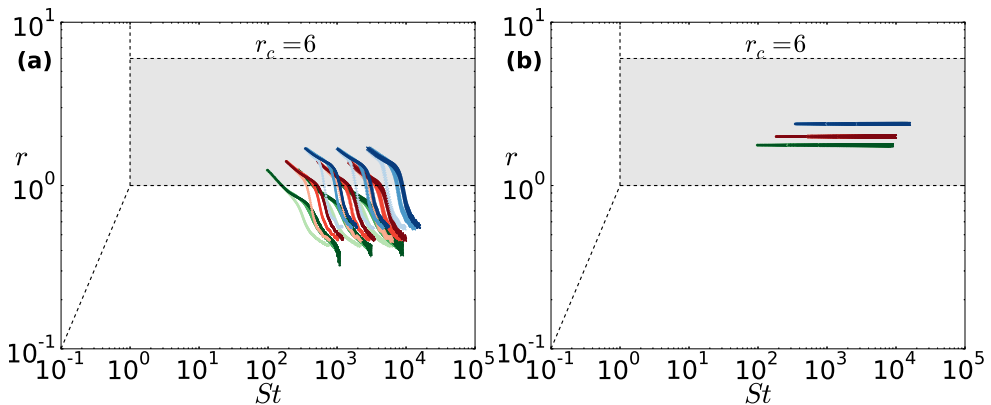


FIGURE 3. Position of all the computed granular rheology points in the  $(St, r)$  plane, considering the drag coefficient taking into account the local hindrance effects (a) and a constant drag coefficient respectively. The dashed lines represent the transition between the different regimes, with a shaded area between the expected transition from turbulent to free-fall regime  $r_c = 1$  and the one estimated by Courrech du Pont *et al.* (2003)  $r_c = 6$ .

us to obtain the granular rheology for a wide range of inertial numbers from a unique simulation. Performing simulations with variation of  $\rho_p$ ,  $d$  and  $h$  the water depth, the results take the form of a set of  $\mu(I)/\phi(I)$  curves sampling the parameter space. In the present paper, each simulation will be represented by a colored symbol, where the symbol is associated with the particle diameter  $d$ , its color is associated with the value of the specific density  $\rho_p/\rho_f - 1$  and its shading represents the Shields number (the darker the colour, the higher the Shields number) (see table 2).

### 3.2. Results

The influence of the interstitial fluid on the granular rheology varies between and within the different configurations investigated and one might expect transitions between the different regimes of the  $\mu(I)$  rheology (free-fall, turbulent, viscous). While generally of minor importance, the choice for the computation of the Stokes and  $r$  dimensionless numbers (eq. 1.4 and 1.5) becomes crucial when approaching a transition between two regimes, as in the present analysis. In order to define accurately the different regimes and to impose that the transition from the viscous to the turbulent regime depends only on the particle Reynolds number ( $Re_p = St/r$ ), the limit turbulent drag coefficient  $C_D^\infty = 0.44$  should be considered and both turbulent and viscous drag forces should be taken without the contribution from hindrance effects. However, the classical picture of the  $\mu(I)$  rheology associates the inertial number with a time-scale ratio representative of the local rearrangement process (Andreotti *et al.* 2013), which is affected by hindrance effects and the particle Reynolds number in the low- $Re_p$  limit of the turbulent regime ( $Re_p \in [1, 10^4]$ ). Focusing on the present case ( $St \gg 1$  and  $r \sim 1$  so that  $Re_p \gg 1$ ), the  $r$  and turbulent inertial numbers have been computed from a constant drag coefficient taking into account the local hindrance effects  $C_D(z) = C_D^\infty(1 - \phi(z))^{-3.1}$ , putting aside the considerations on the transition from the viscous to the turbulent regime.

Figure 3a shows the parameter variation in the  $St/r$  plane. According to the estimation of Courrech du Pont *et al.* (2003) ( $r_c \sim 6$ ), all of the data belong to the turbulent regime and should show a collapse as a function of the turbulent inertial number. As can be seen from figure 3b, this would also be the case if the  $r$  number was evaluated without

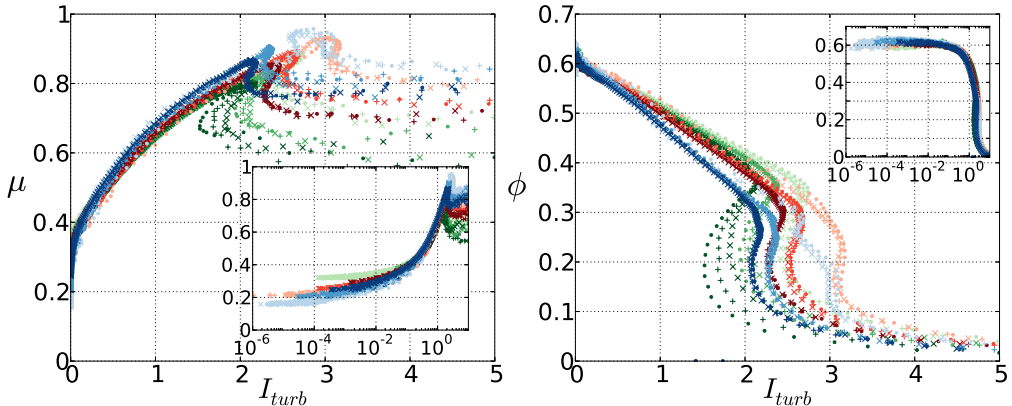


FIGURE 4. Shear to normal stress ratio  $\mu = \tau^p/P^p$  and solid volume fraction  $\phi$  as a function of the turbulent inertial number  $I_{turb} = \dot{\gamma}d\sqrt{\rho^f C_D}/P^p$ , for all the cases presented in table 2 with variation of Shields number, specific density and particle diameter.

taking into account the local hindrance effect.

Figure 4 and 5 show the shear to normal stress ratio and the solid volume fraction as a function of the turbulent inertial number and the dry inertial number respectively. Both figures exhibit a data collapse over the range  $I \in [10^{-2}, 0.1]$ . At higher inertial numbers however, the data split apart as a function of the turbulent inertial number, while the collapse persists up to  $I_{dry} \sim 2$  for the dry inertial number case. Therefore, the configurations sampled are better described by the dry inertial number and belong at first order to the free-fall regime, in contradiction with the predicted transition from the free-fall to the turbulent regimes of Courrech du Pont *et al.* (2003). One still notes a slight dependence on the specific density in figure 5, suggesting a second-order influence of the fluid inertial rearrangement mechanism. This absence of clear transition from the free-fall to the turbulent regimes is consistent with recent global analysis of immersed granular collapse using a DNS-DEM model (Izard *et al.* 2014). Similarly to the transition from the viscous to the free-fall regime (Trulsson *et al.* 2012), one might expect the transition region to be described by a combination of the turbulent and dry inertial numbers. In the present paper, the second-order effects are neglected for simplicity and the dry inertial number will be adopted in the following.

Coming back to figure 5 and considering the semi-logarithmic scale insets, the solid volume fraction curves are seen to collapse down to the lowest inertial number sampled ( $I_{dry} \sim 10^{-5}$ ). For the shear to normal stress ratio, the different curves split apart below  $I_{dry} \sim 10^{-2}$ , following different branches depending on both the specific density and the Shields number of the run considered. No variation with the particle diameter is observed. In all cases, the stress ratio values in this region are below the expected static effective friction coefficient of the granular medium ( $\mu_s \sim 0.38$  for monodisperse glass beads (Andreotti *et al.* 2013)). This low-inertial-number region corresponds to the lower parts of the different simulations where a creeping regime is observed with the solid velocity following an exponential decrease (Maurin *et al.* 2015; Houssais *et al.* 2015) similar to the one observed in dry granular flows on a heap (Komatsu *et al.* 2001; Richard *et al.* 2008). These two features are characteristic of non-local effects (e.g. Kamrin & Koval (2012); Bouzid *et al.* (2013)), where the granular flow is influenced by the far field, i.e. by the top granular flow in the present configuration. Despite the

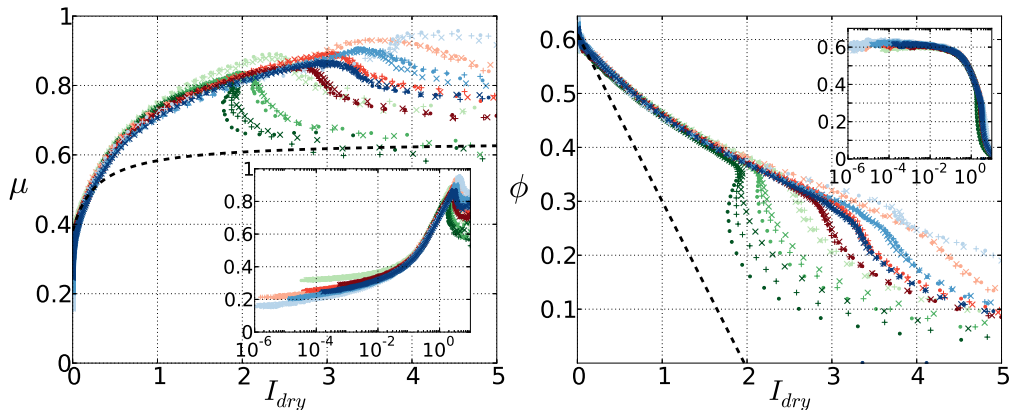


FIGURE 5. Shear to normal stress ratio  $\mu = \tau^p/P^p$  and solid volume fraction  $\phi$  as a function of the dry inertial number  $I_{dry} = \dot{\gamma}d\sqrt{\rho^p/P^p}$  for all the cases presented in table 2 with variation of Shields number, specific density and particle diameter. The parameters of the simulation sampled and the corresponding symbols are shown in table 2. The dashed lines (—) represents the classical expression of  $\mu(I)/\phi(I)$  (eq. 1.2 and 1.3) with the parametrization of Da Cruz *et al.* (2005) and Jop *et al.* (2006):  $\mu_s = 0.38$ ,  $\mu_2 = 0.64$ ,  $I_0 = 0.279$ ,  $a = 0.31$ .

interest for granular media and out-of-equilibrium configurations, the quasi-static part of bedload transport does not contribute significantly to the sediment transport rate and will not be investigated further in this paper.

Toward the upper limit, the data are seen to collapse up to  $I_{dry} \sim 2$  for both the solid volume fraction and the shear to normal stress ratio (figure 5). At higher inertial numbers, the different curves - corresponding to the different simulations - progressively exhibit a transition to a different behaviour characterised by a decrease of the shear to normal stress ratio, and a slope break on the solid volume fraction versus inertial number curves.

The observed decrease in the shear to normal stress ratio as a function of the inertial number is characteristic of the transition from dense to dilute granular behaviour (Forterre & Pouliquen 2008). In the present results, the position of the transition in terms of inertial number is particularly high ( $I \sim 2-3$ ) and depends on the configurations sampled (figure 5). At such a high inertial number, the restitution coefficient is seen to have a non-negligible effect on the rheological curves (see figure 6). Focusing on the classical dry granular flow literature (e.g. Da Cruz *et al.* (2005); Jop *et al.* (2006); Forterre & Pouliquen (2008); Jop (2015)), the  $\mu(I)$  approach is considered to break down above  $I_{dry} \sim 0.5$  for glass beads, when collisional mechanisms comes into play (Da Cruz *et al.* 2004; Lois *et al.* 2006; Forterre & Pouliquen 2008). Therefore, it is unable to explain both the observed variation of the transition position at constant restitution coefficient and the collapse observed in regions where collisional mechanisms contribute non-negligibly to the rheology.

Recently, similar persistence of dense granular flow behaviour at high inertial numbers has been observed in inclined plane configurations. Holyoake & McElwaine (2012) observed experimentally dense granular flows up to inertial numbers  $I_{dry} \sim 2$  in steady non-uniform dry granular flows of sand in a steep channel with lateral walls and a bumpy base. Moreover, analyzing granular roll wave instabilities using the DEM, Börzsönyi *et al.* (2009) computed the local granular rheology and obtained a collapse of their

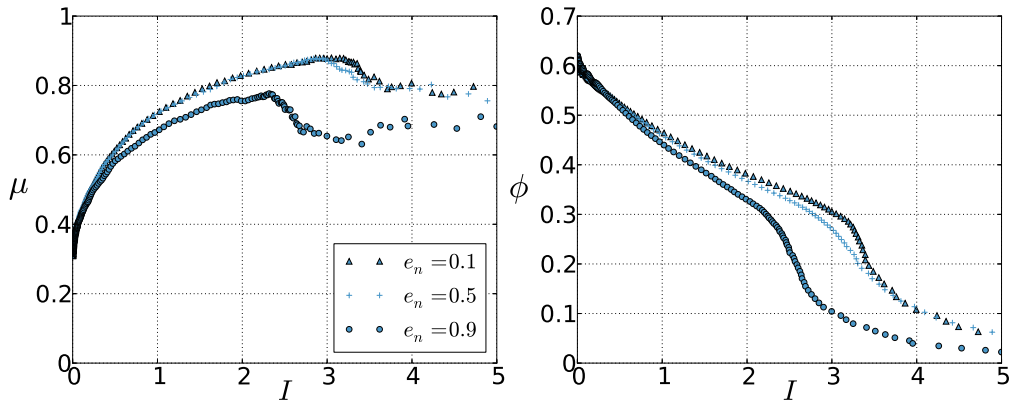


FIGURE 6. Effect of the restitution coefficient on the shear to normal stress ratio  $\mu = \tau^p/P^p$  and solid volume fraction  $\phi$  as a function of the dry inertial number  $I_{dry} = \dot{\gamma}d\sqrt{\rho^p/P^p}$  for a representative case (case r2d6s2 in table 2).

rheological data up to  $I_{dry} \sim 1$ . In these two configurations as well as in the present study, the complexity of the granular flow considered can lead to differences with respect to the simple shear picture. In particular, the local analysis of spatially non-homogeneous granular flows made in the present paper and in Börzsönyi *et al.* (2009), might lead to secondary gradient effects that are not taken into account in the  $\mu(I)$  rheology. Therefore, the local character of the analysis and/or the specificity of the configuration seem to affect the persistence of a dense granular flow at high inertial numbers.

As a consequence of the high-inertial-numbers collapse, the classical  $\mu(I)/\phi(I)$  expressions (eq. 1.2 and 1.3) and parametrisation do not fit the present results well at high inertial numbers (see the fit of Jop *et al.* (2006) in figure 5). Indeed, the collisional contribution becomes important in this region and one might need to extend the  $\mu(I)/\phi(I)$  relationships as done by Holyoake & McElwaine (2012) for the inclined plane configuration.

The results have evidenced the ability of the  $\mu(I)$  framework to describe the granular flow rheology in bedload transport in the dense granular flow region. They have shown that the interstitial fluid does not influence the dense granular rheology importantly and that the fluid flow acts mainly as an external forcing in turbulent bedload transport. In addition, the analysis has underlined the variety and the complexity of the granular behaviours observed in bedload transport, which challenge the existing formulation of the  $\mu(I)$  rheology.

#### 4. Granular rheology in bedload transport

The rest of this paper focuses on the analysis of turbulent bedload transport, considering realistic conditions typical of gravel-bed rivers. Therefore, the specific density is taken as  $\rho^p/\rho^f - 1 = 1.5$  and additional DEM simulations are performed at Shields numbers down to the onset of motion. The analysis of the DEM results allows us to propose a  $\mu(I)$ -based granular rheology for turbulent bedload transport. The relevance of the proposed granular rheology is further tested in a second time, using the Eulerian-Eulerian model presented in section 2.

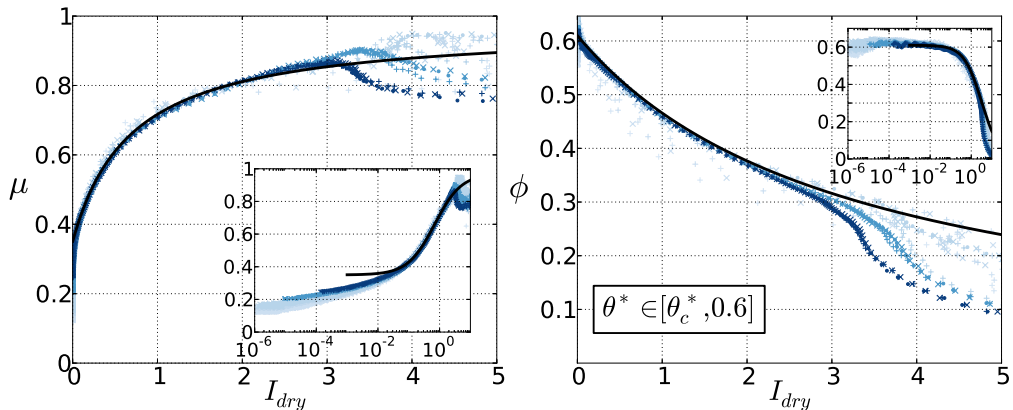


FIGURE 7. Shear to normal stress ratio and solid volume fraction as a function of the dry inertial number, for realistic bedload transport simulations with specific density  $\rho^p/\rho^f - 1 = 1.5$ , Shields number from incipient motion to 0.7, and particle diameter of  $d = 3\text{mm}$ ,  $d = 6\text{mm}$ , and  $d = 12\text{mm}$ . The black lines represent the best fit obtained with equations 1.2 and 4.1 ( $\mu_1 = 0.38$ ,  $\mu_2 = 0.64$ ,  $I_0 = 0.279$ ,  $\phi^{max} = 0.61$ , and  $b = 0.31$ ). The symbols colors are function of the simulation Shields number: the darkest the color, the highest the Shields number.

#### 4.1. Parametrisation of the $\mu(I)$ rheology

Figure 7 shows the granular shear to normal stress ratio and the solid volume fraction as a function of the inertial number, for simulations with Shields numbers from  $\theta^* = 0.04$  to  $\theta^* = 0.6$  and for particle diameters  $d \in \{3; 6; 12\}$  mm. In these new configurations closer to realistic bedload transport, most of the data are seen to collapse for both the solid volume fraction and the granular stress ratio up to high inertial numbers. Above  $I \sim 3$  and under  $I \sim 10^{-2}$ , the curves split apart similarly to the general case. No dependence upon the particle diameter is observed over the whole range of inertial numbers, pointing out the negligible effect of the  $Re_p$  and  $St$  numbers in the problem. The lowest-Shields-number cases (lightest points) exhibit some specific behaviour with oscillations, lower shear to normal stress ratio and solid volume fraction at given inertial numbers. These cases correspond to the sharpest transitions between a quasi-static granular bed and a few particles in motion on top of it. Therefore, in these configurations the continuous assumption is not strictly valid and the limits of the rheological description are reached.

Overriding these limitations close to the critical Shields number and assuming that the high-inertial-numbers granular behaviour is not dominant in bedload transport, the  $\mu(I)$  constitutive laws are pragmatically best-fitted on the Eulerian-Lagrangian simulation results over the range of inertial numbers  $I_{dry} \in [10^{-2}, 3]$ . The classical solid volume fraction expression (eq. 1.3) predicts negative values at high inertial numbers and is unable to describe the present results. Consequently, the expression is modified and is chosen following Aussillous *et al.* (2013) and Revil-Baudard & Chauchat (2013) as

$$\phi(I) = \frac{\phi^{max}}{1 + bI}. \quad (4.1)$$

The best fits of equations 1.2 and 4.1 on the data give the following parameters:  $b = 0.31$ ,  $\mu_s = 0.35$ ,  $\mu_2 = 0.97$  and  $I_0 = 0.69$ , with  $\phi^{max}$  imposed to take the value measured in the Eulerian-Lagrangian simulations:  $\phi^{max} = 0.61$ . Developing the solid volume fraction expression around  $I = 0$ , the value of  $b$  obtained is consistent with both the

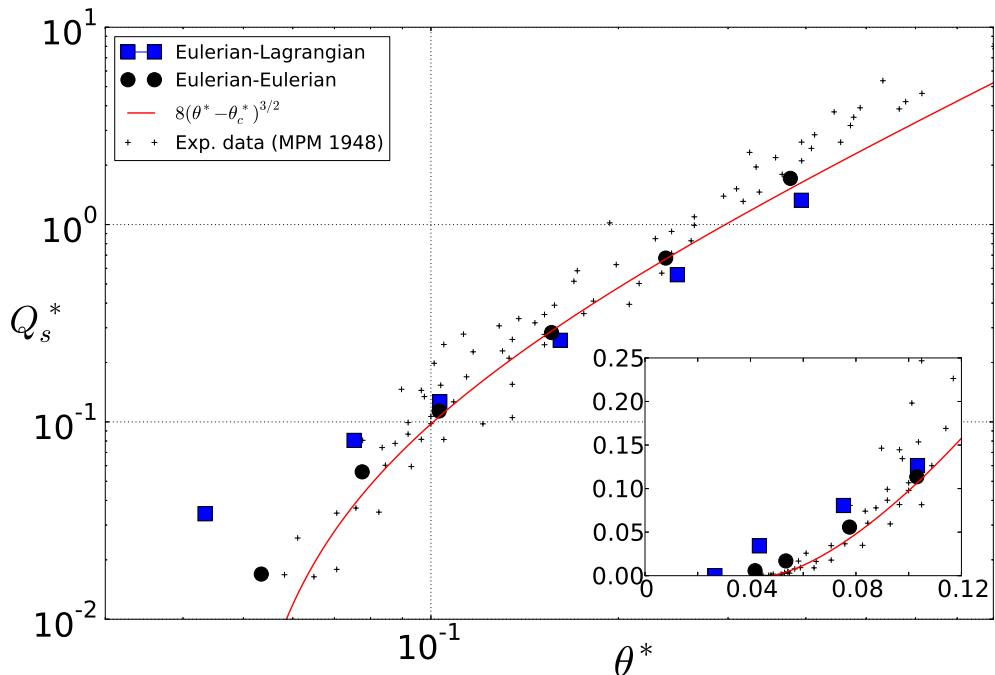


FIGURE 8. Dimensionless sediment transport rate as a function of the Shields number for two-phase continuous simulations (Eulerian-Eulerian) and coupled fluid-discrete element simulations (Eulerian-Lagrangian), with realistic parameters for turbulent bedload transport:  $\rho^p/\rho^f - 1 = 1.5$  and  $d = 6\text{mm}$ . The black crosses and the red line represent the data and the fit of Meyer-Peter & Müller (1948) respectively.

parametrisation of Da Cruz *et al.* (2005) in the dry regime and the one from Boyer *et al.* (2011) and Trulsson *et al.* (2012) in the viscous regime. The values of  $\mu_2$  and  $I_0$  are logically higher than in the original  $\mu(I)$  rheology, as no real saturation of the stress ratio is observed in our data. The best fits describe very well the results obtained within the collapsing range of  $I_{dry}$ , as can be seen in figure 7. Outside this interval, they do not reproduce the non-local effects at low inertial numbers ( $I_{dry} < 10^{-2}$ ) and the drop in both the shear to normal stress ratio and the solid volume fraction for  $I_{dry} > 3$ .

Assuming the dense granular behaviour to be dominant, the two relationships (eq. 1.2-4.1) together with the values determined from the best fits are proposed as a  $\mu(I)$ -based granular rheology for turbulent bedload transport.

#### 4.2. Eulerian-Eulerian simulations

In order to evaluate the relevance of the proposed granular rheology it has been implemented in the Eulerian-Eulerian model presented in section 2. Simulations have been performed using exactly the same parameters for both the Eulerian-Lagrangian and the Eulerian-Eulerian models ( $\rho_p/\rho_f - 1 = 1.5$ ;  $d = 6\text{ mm}$ ,  $\alpha = 0.05$ ,  $h$ ). The particle diameter has been varied ( $d \in 3, 6, 12\text{mm}$ ) but does not influence the results so that only the case  $d = 6\text{mm}$  is presented for clarity.

Figure 8 presents the dimensionless sediment transport rate versus the Shields number for the Eulerian-Eulerian model, the Eulerian-Lagrangian model and the experimental data and empirical law of Meyer-Peter & Müller (1948). A good agreement with the



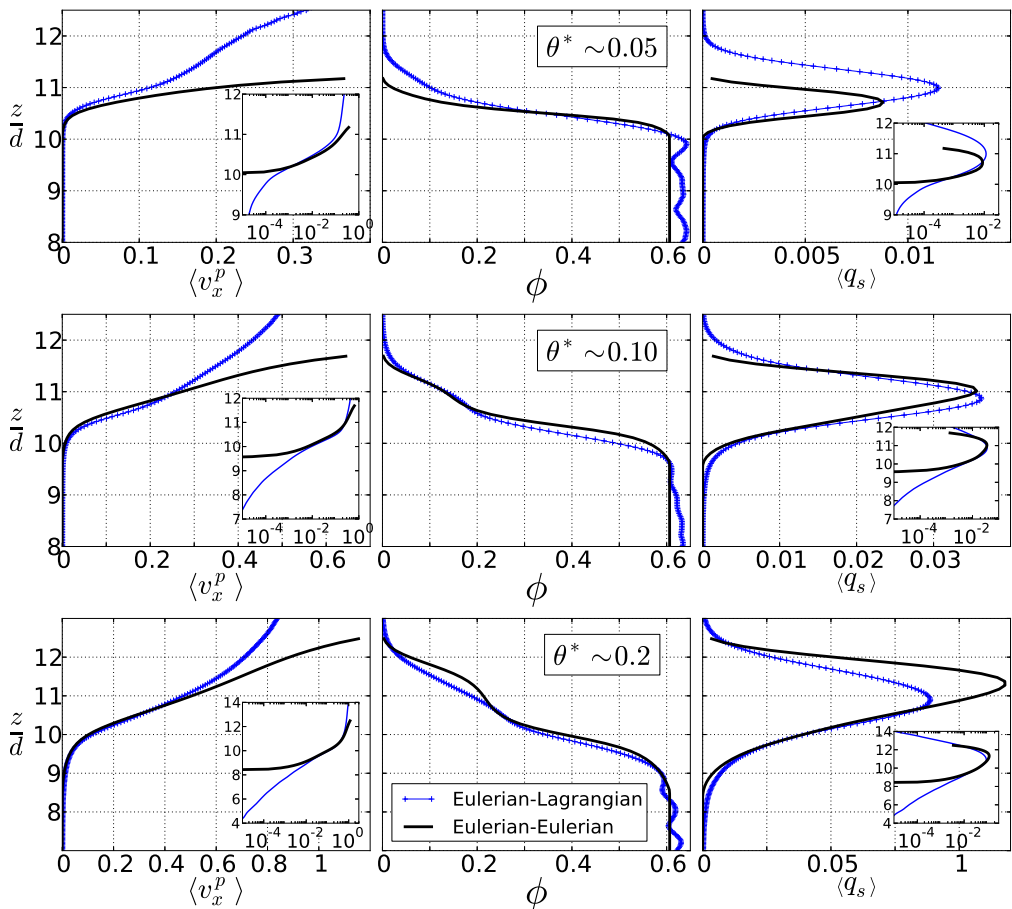


FIGURE 9. Solid depth profile comparison between the two-phase continuous model (Euler-Euler) and the coupled fluid-discrete element model (Euler-Lagrange) for three different Shields number  $\theta^*$  with  $d = 6\text{mm}$  and  $\rho^p/\rho^f - 1 = 1.5$ . Solid velocity  $\langle v_x^p \rangle^s$  and transport rate density  $\langle q_s \rangle^s$  are expressed in  $\text{m/s}$  while the solid volume fraction is dimensionless. The fluid mechanics convention is used.

experimental data is obtained using both models. The proposed granular rheology enables the Eulerian-Eulerian model to accurately reproduce the critical Shields number ( $\theta_c^* \sim 0.04$ ) and the global trend over a wide range of Shields numbers ( $\theta^* \in [\theta_c^*, 0.7]$ ). Quite surprisingly, the Eulerian-Eulerian model better predicts the smooth transition around the critical Shields number, in a region where the continuous assumption breaks down. Conversely, at high Shields numbers the increased importance of the dilute region, which is not well described by the proposed rheology (section 4.1), induces a slight discrepancy between the Eulerian-Eulerian and Eulerian-Lagrangian models.

To go further in the analysis, the comparison is extended to the granular depth profiles by decomposing the sediment transport rate into the integral of the sediment transport rate density  $\langle q_s \rangle(z) = \langle v_x \rangle^s(z) \phi(z)$  (Bagnold 1956):

$$Q_s = \int_0^\infty \langle q_s \rangle(z) dz = \int_0^\infty \langle v_x \rangle^s(z) \phi(z) dz. \quad (4.2)$$

Figure 9 shows the comparison of the solid volume fraction, the solid velocity and the transport rate density profiles obtained with the Eulerian-Eulerian and Eulerian-Lagrangian models for three different Shields numbers  $\theta^* = \{0.05; 0.1; 0.2\}$ . The Eulerian-Eulerian model reproduces accurately the granular depth profiles obtained with the Eulerian-Lagrangian model for solid volume fractions approximately higher than 0.3 ( $\phi \gtrsim 0.3$ ). This value roughly corresponds to the domain for which the proposed granular rheology describes the Eulerian-Lagrangian results very well (see figure 7). Only the lower quasi-static velocity profile - negligible in terms of sediment transport rate - is not reproduced, as non-local effects have not been taken into account in the granular rheology. In the dilute region ( $\phi \lesssim 0.3$ ), the particle velocity is overestimated by the Eulerian-Eulerian model for the three different Shields numbers, showing an increasing discrepancy toward the lower solid volume fraction region. This is associated with an under-estimation of the solid volume fraction close to incipient motion and an over-estimation at high Shield numbers. These behaviours point out both the ill-posedness of the  $\mu(I)$  rheology as the solid volume fraction goes to zero and the inability of the proposed rheology to describe the dilute region accurately. Despite these limitations, the good lower boundary condition given by the accurate description of the dense granular flow constrains the dilute behaviour and enables a good description of the sediment transport rate over a wide range of Shields numbers with the Eulerian-Eulerian model.

The present results show that a  $\mu(I)$  rheology is able to reproduce the main features of turbulent bedload transport in terms of sediment transport rate and dense granular depth profiles, in steady uniform configurations. Considering the much lower computational cost of Eulerian-Eulerian simulations compared with Eulerian-Lagrangian ones, it will allow an important step to be made in the upscaling process towards applications. In this perspective, the fluid phase description might have to be upgraded, using a two-equation turbulence model as  $k - \epsilon$  or  $k - \omega$  (Hsu *et al.* 2004; Amoudry 2014; Lee *et al.* 2016), or eddy resolving simulations.

## 5. Summary and conclusion

The granular rheology in idealised turbulent bedload transport has been studied using a coupled fluid-discrete-element model. Computing the granular stress tensor locally as a function of the depth and performing simulations for various Shields numbers, specific densities and particle diameters, the data have been shown to collapse over an important range of inertial numbers, demonstrating the relevance of the  $\mu(I)$  rheology for turbulent bedload transport description. No clear transition from the free-fall to the turbulent regime of the  $\mu(I)$  rheology has been observed, supporting recent numerical observations and suggesting that the interstitial fluid does not importantly influence the granular rheology in turbulent bedload transport. In addition, consistently with recent literature, the data have been observed to collapse in terms of both the solid volume fraction and the shear to normal stress ratio, up to inertial numbers as high as  $I \sim 2$ . The persistence of a dense granular flow behaviour at such a high inertial number together with the observed progressive transition from dense to dilute behaviour challenges the classical conceptions and parametrizations of the  $\mu(I)$  rheology, and opens interesting perspectives for a better understanding of granular media rheology at high inertial numbers. Beyond these observations, a  $\mu(I)$ -based granular rheology has been fitted to the present Eulerian-Lagrangian bedload transport simulations. The proposed rheology has been successfully tested using a Eulerian-Eulerian model. It has been shown to accurately reproduce the dense granular depth profiles and the classical experimental results in terms of sediment

transport rate from the onset of motion up to a Shields number of  $\theta^* \sim 0.7$ .

Further work is needed to better understand the high-inertial-numbers behaviour and extend the granular rheology to the description of the dilute region. At this stage it is not clear whether the  $\mu(I)$  rheology could be extended to handle this regime transition. Besides, the proposed rheology can already be used in three dimensional Eulerian-Eulerian numerical models and represents a step in the upscaling process from particle-scale simulations toward full-scale problem modelling.

## Acknowledgement

We are grateful to the three anonymous reviewers for relevant and constructive questions, and to Ashley Dudill for English corrections. RM would like to thank Thierry Faug for fruitful discussions. This research was supported by Irstea (formerly Cemagref), the labex OSUG@2020 and the French Institut National des Sciences de l'Univers programs EC2CO-BIOHEFECT and EC2CO-LEFE MODSED.

## Appendix A. Momentum balance derivation

In order to validate the stress tensor profile computed, the momentum balance is analyzed in the framework of the continuous two-phase equations (Jackson 2000). In the present appendix, the equations are derived and integrated to show the exact terms computed in the body of the paper. Using the steady and uniform character of the problem considered, the momentum balances for both the fluid and the granular phases read along the streamwise direction (Jackson 2000)

$$0 = \frac{\partial S_{xz}^f}{\partial z} + \frac{\partial R_{xz}^f}{\partial z} + \rho^f (1 - \phi) g \sin \alpha - n \left\langle f_{fx}^p \right\rangle^p, \quad (\text{A } 1)$$

$$0 = \frac{\partial \tau_{xz}^p}{\partial z} + \rho^p \phi g \sin \alpha + n \left\langle f_{fx}^p \right\rangle^p. \quad (\text{A } 2)$$

Combining these two equations together, the mixture momentum balance can be written as

$$0 = \frac{\partial S_{xz}^f}{\partial z} + \frac{\partial R_{xz}^f}{\partial z} + \frac{\partial \tau_{xz}^p}{\partial z} + (\rho^p \phi + (1 - \phi) \rho^f) g \sin \alpha. \quad (\text{A } 3)$$

In order to study the stress repartition, the equation is integrated between a given position  $z$  in  $h > z > 0$  and the water free-surface elevation  $h$ , where the viscous, turbulent and particle shear stresses vanish:  $S_{xz}^f(h) = R_{xz}^f(h) = \tau_{xz}^p(h) = 0$ . It leads to the following formulation:

$$0 = -S_{xz}^f(z) - R_{xz}^f(z) - \tau_{xz}^p(z) + g \sin \alpha \left[ \rho^f (h - z) + (\rho^p - \rho^f) \int_z^h \phi dz \right]. \quad (\text{A } 4)$$

From one simulation, it is possible to evaluate all of the terms of the equation at each given elevation. Provided that the stress tensor formulation is appropriate and the system is at equilibrium, the equality should be satisfied.

## REFERENCES

- ŠMILAUER ET AL. 2015 *Yade Documentation 2nd ed. The Yade Project* (<http://yadedem.org/doc/>) DOI: 10.5281/zenodo.34073.
- AMOUDRY, L. O. 2014 Extension of turbulence closure to two-phase sediment transport

- modelling: Application to oscillatory sheet flows. *Advances in Water Resources* **72**, 110–121.
- ANDERSON, T. B. & JACKSON, ROY 1967 Fluid mechanical description of fluidized beds. equations of motion. *Industrial & Engineering Chemistry Fundamentals* **6** (4), 527–539.
- ANDREOTTI, B., FORTERRE, Y. & POULIQUEN, O. 2013 *Granular media: between fluid and solid*. Cambridge University Press.
- ARMANINI, A., CAPART, H., FRACCAROLLO, L. & LARCHER, M. 2005 Rheological stratification in experimental free-surface flows of granular-liquid mixtures. *Journal of Fluid Mechanics* **532**, 269–319.
- ARMANINI, A., LARCHER, M., NUCCI, E. & DUMBSER, M. 2014 Submerged granular channel flows driven by gravity. *Advances in Water Resources* **63**, 1–10.
- AUSSILLOUS, P., CHAUCHAT, J., PAILHA, M., MÉDALE, M. & GUAZZELLI, E. 2013 Investigation of the mobile granular layer in bedload transport by laminar shearing flows. *Journal of Fluid Mechanics* **736**, 594–615.
- BAGNOLD, R. A. 1956 The flow of cohesionless grains in fluids. *Phil Trans R Soc A* **249**, 235–297.
- BERZI, D. & JENKINS, J. T. 2008 A theoretical analysis of free-surface flows of saturated granular-liquid mixtures. *Journal of Fluid Mechanics* **608**, 393–410.
- BERZI, D., DI PRISCO, C. G. & VESCOVI, D. 2011 Constitutive relations for steady, dense granular flows. *Phys. Rev. E* **84**, 031301.
- BÖRZSÖNYI, T., ECKE, R. E. & MCELWAIN, J. N. 2009 Patterns in flowing sand: Understanding the physics of granular flow. *Phys. Rev. Lett.* **103**, 178302.
- BOUZID, M., TRULSSON, M., CLAUDIN, P., CLÉMENT, E. & ANDREOTTI, B. 2013 Nonlocal rheology of granular flows across yield conditions. *Phys. Rev. Lett.* **111**, 238301.
- BOYER, F., GUAZZELLI, É. & POULIQUEN, O. 2011 Unifying suspension and granular rheology. *Phys. Rev. Lett.* **107**, 188301.
- CAMPBELL, C. S. 1990 Rapid granular flows. *Annual Review of Fluid Mechanics* **22** (1), 57–90.
- CAPART, H. & FRACCAROLLO, L. 2011 Transport layer structure in intense bed-load. *Geophysical Research Letters* **38** (20), L20402, L20402.
- CASSAR, C., NICOLAS, M. & POULIQUEN, O. 2005 Submarine granular flows down inclined planes. *Physics of Fluids (1994-present)* **17** (10), 103301.
- CHAUCHAT, J., GUILLOU, S., PHAM VAN BANG, D. & DAN NGUYEN, K. 2013 Modelling sedimentation-consolidation in the framework of a one-dimensional two-phase flow model. *Journal of Hydraulic Research* **51** (3), 293–305.
- CHAUCHAT, J., REVEL-BAUDARD, T. & HURTER, D. 2015 An improved two-phase flow model for steady uniform sheet-flow based on dense granular flow rheology. In *36th IAHR world Congress*. The Hague, The Netherlands.
- CHIODI, F., CLAUDIN, P. & ANDREOTTI, B. 2014 A two-phase flow model of sediment transport: transition from bedload to suspended load. *Journal of Fluid Mechanics* **755**, 561–581.
- COWEN, E. A., DUDLEY, R. D., LIAO, Q., VARIANO, E. A. & LIU, P. L.-F. 2010 An insitu borescopic quantitative imaging profiler for the measurement of high concentration sediment velocity. *Experiments in Fluids* **49** (1), 77–88.
- DA CRUZ, F., CHEVOIR, F., ROUX, JN. & IORDANOFF, I. 2004 Macroscopic friction of dry granular materials. In *Transient processes in tribology* (ed. G Dalmaz, AA Lubrecht, D Dowson & M Priest), *Tribology and Interface Engineering Series*, vol. 43, pp. 53–61. 30th Leeds-Lyon Symposium on Tribology, Inst Natl Sci Appl, Lyon, FRANCE, SEP 02-05, 2003.
- DA CRUZ, F., EMAM, S., PROCHNOW, M., ROUX, J-N. & CHEVOIR, F. 2005 Rheophysics of dense granular materials: Discrete simulation of plane shear flows. *Phys. Rev. E* **72**, 021309.
- DALLAVALLE, J. M. 1948 *Micrometrics : The technology of fine particles*, , vol. 2nd edition. Pitman Pub. Corp.
- DOPPLER, D., GONDRET, P., LOISELEUX, T., MEYER, S. & RABAUD, M. 2007 Relaxation dynamics of water-immersed granular avalanches. *Journal of Fluid Mechanics* **577**, 161–181.
- DURAN, O., ANDREOTTI, B. & CLAUDIN, P. 2012 Numerical simulation of turbulent sediment transport, from bed load to saltation. *Physics of Fluids* **24** (10), 103306.

- EINSTEIN, HA. 1942 Formulas for the transport of bed sediment. *Transactions of the American Society of Civil Engineers* **107**, 561–574.
- FORTERRE, Y. & POULIQUEN, O. 2008 Flows of dense granular media. *Annual Review of Fluid Mechanics* **40** (1), 1–24.
- FREDSØE, J. & DEIGAARD, R. 1992 *Mechanics of Coastal Sediment Transport*. World Scientific.
- FREY, P. 2014 Particle velocity and concentration profiles in bedload experiments on a steep slope. *Earth Surface Processes and Landforms* **39** (5), 646–655.
- FREY, P. & CHURCH, M. 2009 How river beds move. *Science* **325**, 1509–1510.
- FREY, P. & CHURCH, M. 2011 Bedload : a granular phenomenon. *Earth Surface Processes and Landform* **36**, 58–69.
- GOLDHIRSCH, I. 2003 Rapid granular flows. *Annual Review of Fluid Mechanics* **35** (1), 267–293.
- GOLDHIRSCH, I. 2010 Stress, stress asymmetry and couple stress: from discrete particles to continuous fields. *Granular Matter* **12** (3), 239–252.
- HERGAULT, V., FREY, P., MÉTIVIER, F., BARAT, C., DUCOTTET, C., BÖHM, T. & ANCEY, C. 2010 Image processing for the study of bedload transport of two-size spherical particles in a supercritical flow. *Experiments in Fluids* **49** (5), 1095–1107.
- HOLYOAKE, A.J. & MCELWAINE, J. N. 2012 High-speed granular chute flows. *Journal of Fluid Mechanics* **710**, 35–71.
- HOUSSAIS, M., ORTIZ, C. P., DURIAN, D. J. & JEROLMACK, D. J. 2015 Onset of sediment transport is a continuous transition driven by fluid shear and granular creep. *Nature communications* **6**, 6527.
- HSU, T. J., JENKINS, J. T. & LIU, P. L. F. 2004 On two-phase sediment transport: sheet flow of massive particles. *Proceedings of the Royal Society of London Series A-mathematical Physical and Engineering Sciences* **460** (2048), 2223–2250.
- IZARD, E., BONOMETTI, T. & LACAZE, L. 2014 Simulation of an avalanche in a fluid with a soft-sphere/immersed boundary method including a lubrication force. *The Journal of Computational Multiphase Flows* **6** (4), 391–406.
- JACKSON, R. 2000 *The dynamics of fluidized particles*. Cambridge University Press.
- JENKINS, J.T. & HANES, D.M. 1998 Collisional sheet flows of sediment driven by a turbulent fluid. *Journal of Fluid Mechanics* **370**, 29–52.
- JENKINS, J. T. 2006 Dense shearing flows of inelastic disks. *Physics of Fluids* **18** (10), 103307.
- JENKINS, J. T. 2007 Dense inclined flows of inelastic spheres. *Granular Matter* **10** (1), 47–52.
- JI, C., MUNJIZA, A., AVITAL, E., MA, J. & WILLIAMS, J. J. R. 2013 Direct numerical simulation of sediment entrainment in turbulent channel flow. *Physics of Fluids* **25** (5), 056601.
- JOP, P. 2015 Rheological properties of dense granular flows. *Comptes rendus physique* **16** (1), 62–72.
- JOP, P., FORTERRE, Y. & POULIQUEN, O. 2006 A constitutive law for dense granular flows. *Nature* **441** (7094), 727–730.
- KAMRIN, K. & KOVAL, G. 2012 Nonlocal constitutive relation for steady granular flow. *Phys. Rev. Lett.* **108**, 178301.
- KIDANEMARIAM, A G. & UHLMANN, M. 2014 Interface-resolved direct numerical simulation of the erosion of a sediment bed sheared by laminar channel flow. *International Journal of Multiphase Flow* **67** (0), 174 – 188.
- KOMATSU, T. S., INAGAKI, S., NAKAGAWA, N. & NASUNO, S. 2001 Creep motion in a granular pile exhibiting steady surface flow. *Phys. Rev. Lett.* **86**, 1757–1760.
- LAJEUNESSE, E., MALVERTI, L. & CHARRU, F. 2010 Bed load transport in turbulent flow at the grain scale: Experiments and modeling. *Journal of Geophysical Research: Earth Surface* **115**, F04001.
- LARCHER, M., FRACCAROLLO, L., ARMANINI, A. & CAPART, H. 2007 Set of measurement data from flume experiments on steady uniform debris flows. *Journal of Hydraulic Research* **45**, 59–71.
- LEE, CHENG-HSIEN, LOW, YING MIN & CHIEW, YEE-MENG 2016 Multi-dimensional rheology-based two-phase model for sediment transport and applications to sheet flow and pipeline scour. *Physics of Fluids* **28** (5).
- LI, L. & SAWAMOTO, M. 1995 Multi-phase model on sediment transport in sheet-flow regime under oscillatory flow. *Coastal engineering Japan* **38**, 157–178.

- LOIS, G., LEMAÎTRE, A. & CARLSON, J. M. 2006 Emergence of multi-contact interactions in contact dynamics simulations of granular shear flows. *Europhys. Lett.* **76** (2), 318–324.
- MAURIN, R. 2015 Investigation of granular behavior in bedload transport using an Eulerian-Lagrangian model. PhD thesis, Université Grenoble Alpes.
- MAURIN, R., CHAUCHAT, J., CHAREYRE, B. & FREY, P. 2015 A minimal coupled fluid-discrete element model for bedload transport. *Physics of Fluids* **27** (11), 113302.
- MEYER-PETER, E. & MÜLLER, R. 1948 Formulas for bed-load transport. In *Proc. 2nd Meeting*, pp. 39–64. IAHR.
- MIDI, GDR 2004 On dense granular flows. *The European Physical Journal E* **14** (4), 341–365.
- MOUILLERON, H., CHARRU, F. & EIFF, O. 2009 Inside the moving layer of a sheared granular bed. *Journal of Fluid Mechanics* **628**, 229–239.
- OURIEMI, M., AUSSILLOUS, P. & GUAZZELLI, E. 2009 Sediment dynamics. part 1. bed-load transport by laminar shearing flows. *Journal of Fluid Mechanics* **636**, 295–319.
- COURRECH DU PONT, S., GONDRET, P., PERRIN, B. & RABAUD, M. 2003 Granular avalanches in fluids. *Phys. Rev. Lett.* **90**, 044301.
- PRANDTL, L. 1926 Bericht über neuere Turbulenzforschung. *Hydraulische Probleme. Vorträge Hydrauliktagung Göttingen* **5**, 1–13.
- REVIL-BAUDARD, T. & CHAUCHAT, J. 2013 A two-phase model for sheet flow regime based on dense granular flow rheology. *Journal of Geophysical Research: Oceans* **118** (2), 619–634.
- REVIL-BAUDARD, T., CHAUCHAT, J., HURTHER, D. & BARRAUD, P-A. 2015 Investigation of sheet-flow processes based on novel acoustic high-resolution velocity and concentration measurements. *Journal of Fluid Mechanics* **767**, 1–30.
- RICHARD, P., VALANCE, A., MÉTAYER, J.-F., SANCHEZ, P., CRASSOUS, J., LOUGE, M. & DELANNAY, R. 2008 Rheology of confined granular flows: Scale invariance, glass transition, and friction weakening. *Phys. Rev. Lett.* **101**, 248002.
- RICHARDSON, J. F. & ZAKI, W. N. 1954 Sedimentation and fluidization: Part i. *Trans. Instn. Chem. Engrs* **32**.
- RONDON, L., POULIQUEN, O. & AUSSILLOUS, P. 2011 Granular collapse in a fluid: Role of the initial volume fraction. *Physics of Fluids* **23** (7), 073301.
- ROUX, J-N. & COMBE, G. 2002 Quasistatic rheology and the origins of strain. *Comptes Rendus Physique* **3** (2), 131 – 140.
- SCHWAGER, T. & PÖSCHEL, T. 2007 Coefficient of restitution and linear spring-dashpot model revisited. *Granular Matter* **9**, 465–469.
- SUMER, B. M., KOZAKIEWICZ, A., FREDSSØE, J. & DEIGAARD, R. 1996 Velocity and concentration profiles in sheet-flow layer of movable bed. *Journal of Hydraulic Engineering* **122** (10), 549–558.
- TRULSSON, M., ANDREOTTI, B. & CLAUDIN, P. 2012 Transition from the viscous to inertial regime in dense suspensions. *Phys. Rev. Lett.* **109**, 118305.